How to cite: *Angew. Chem. Int. Ed.* **2025**, *64*, e202424694
doi.org/10.1002/anie.202424694

Luminescence **Very Important Paper**

Iridium(III) Carbene Complexes Featuring Either Metal-to-Ligand Charge Transfer (MLCT) or Through-Space Charge Transfer (TSCT) Blue Luminescence

Jie Yan⁺, Yixin Wu⁺, Manli Huang⁺, Lin Cheng⁺, Yi Pan, Chi-Chi Wu, Chia-Hsun Yeh, Jian-Liang Li, Yan-Ding Lin, Yun Chi, Chuluo Yang,* Pi-Tai Chou,* and Kai Chung Lau**

Abstract: Through-space charge transfer (TSCT), rather than the commonly postulated metal-to-ligand charge transfer (MLCT) process, was proposed in getting the lowest lying excited state of newly designed Ir(III) blue phosphors. Accordingly, two benzo[*d*]imidazolylidene pro-chelates, $\mathbf{L12H_2}^+$ and $\mathbf{L13H_2}^+$, one with two cyano groups at the *peri*-benzo and *N*-aryl pendent and the other with its *peri*-cyano group being replaced with methyl substituent, were employed in syntheses of Ir(III) complexes ***f*-ct12b**,**c** and ***f*-ct13b**,**c**. Notably, complexes ***f*-ct12b**,**c** exhibited the traditional MLCT process, while ***f*-ct13b,c** were dominated by the TSCT transition, resulting in a smaller S_1–T_1 energy gap ΔE_{ST}. Next, it prompted us to explore whether their long-lived emission originated from phosphorescence or thermally activated delayed fluorescence (TADF). Although temperature-dependent emission studies favor TADF, the unresolved concerns are still discussed in depth. For application, OLED with the TSCT-based dopant ***f*-ct13b** delivered a maximum external quantum efficiency (EQE) of 22.2% and a max. luminance of 10 000 cd m^{-2}, together with CIE_{xy} of (0.155, 0.120). Moreover, the hyper-OLED with ***f*-ct13c** sensitizer and *ν*-DABNA terminal emitter exhibited a max. EQE of 28.2% and CIE_{xy} of (0.123, 0.129), demonstrating a new approach in developing efficient Ir(III) blue phosphors.

Introduction

Organic light-emitting diodes (OLEDs) already dominate the high-end consumer markets of flat panel displays and monitors, but the industries are still looking for better blue emitters to improve the performances in meeting the future demands and specifications.[1–5] Technically, blue emission possesses higher excitation energy than that of green and red counterparts; therefore, the respective blue emitters will be subject to high stresses and disturbances, including unwanted emission quenching and self-decomposition during operation.[6] This means that efficient and stable blue emitters are still rare and difficult to come by.

Currently, the blue pixels of OLEDs are constructed using fluorophores for their high stability, albeit with relatively inferior efficiency. To conquer this deficiency, scientists have invested considerable efforts in both the thermally activated delayed fluorescence (TADF) materials and transition metal-based phosphors. The former introduces efficient triplet harvesting with reduced singlet-to-triplet energy gap (ΔE_{ST})[7] and the latter exploits heavy-atom-induced fast intersystem crossing to give phosphorescence.[8,9] Both strategies have achieved theoretical unitary internal quantum efficiency. These combined effects have effectively promoted the development of blue OLED technologies. To name a few, Hatakeyama and coworkers pioneered the design of a narrowband TADF emitter *ν*-DABNA, which is capable of exhibiting 469 nm emission with full-width at half-maximum (FWHM) of 18 nm.[10,11] Upon switching to the boron-oxygen-based acceptor, the respective D–A (donor–acceptor) TADF blue emitter gave a high external quantum efficiency (EQE) of 38.2% and low roll-off up to 5000 cd m^{-2}.[12] Later, Adachi reported hyperfluorescent OLEDs with CIE_{xy} of (0.13, 0.16), EQE of 32% at 1000 cd m^{-2}, FWHM of 19 nm, and LT_{95} of 18 h at 1000 cd m^{-2}.[13] For phosphorescent OLEDs, Li and coworkers reported the narrowband blue

[*] J. Yan⁺, Y. Wu⁺, L. Cheng⁺, Y. Pan, Y. Chi, K. C. Lau
Department of Chemistry, Department of Materials Science and Engineering, and Center of Super-Diamond and Advanced Films (COSDAF), City University of Hong Kong, Hong Kong SAR, P.R. China
E-mail: yunchi@cityu.edu.hk
kaichung@cityu.edu.hk

M. Huang⁺, C. Yang
Shenzhen Key Laboratory of New Information Display and Storage Materials, College of Materials Science and Engineering, Shenzhen University, Shenzhen 518055, P.R. China
E-mail: clyang@szu.edu.cn

C.-C. Wu, C.-H. Yeh, J.-L. Li, Y.-D. Lin, P.-T. Chou
Department of Chemistry, National Taiwan University, Taipei 10617, Taiwan
E-mail: chop@ntu.edu.tw

[⁺] These authors contributed equally to this work.

Additional supporting information can be found online in the Supporting Information section

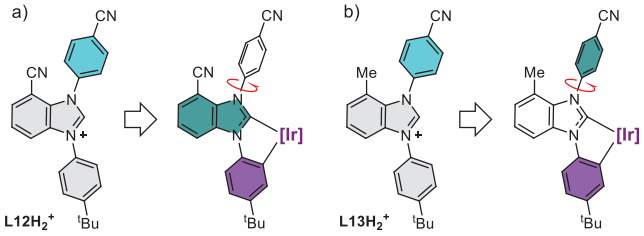

Scheme 1. Structural drawings of carbene chelates **L12H$_2$**$^+$ and **L13H$_2$**$^+$, and the possible electron transition pathway (from purple to olive colored region) in their Ir(III) complexes upon excitation, while the red arrow indicated formation of perpendicularly arranged N-aryl appendages.

Pt(II) emitters with tetradentate chelate,[14] from which the phosphor-sensitized blue OLEDs have clinched LT_{70} of 1113 h[15] and LT_{95} of 72.9 h at 1000 cd m^{-2}.[16] Independently, Lee demonstrated that the blue devices with Ir(III) phosphor Ir(cb)$_3$ doped in an electroplex host have achieved remarkable performances with CIE_{xy} of (0.12, 0.13), EQE_{max} of 27.6%, and LT_{50} of 10^4 h at 100 cd m^{-2}.[17]

From the materials perspective, we speculated that the transition metal blue phosphors may be comparable or even better than TADF emitters. Also, Ir(III) phosphors should also surpass all other transition metal-based phosphors according to the following facts.

(i) Despite a very high max. EQE, most TADF emitters showed a relatively small J_{90} value, defined as the current density at which the EQE falls to 90% of its peak value.[18] It means they probably cannot work under the high current density. On the other hand, phosphors tend to possess higher J_{90} due to the faster radiative transition and lower exciton density at the higher current densities.[19] Particularly, if they were employed as sensitizers to convey their energy to terminal fluorescent emitters via Förster resonance energy transfer (FRET) due to the partially allowed $T_1 \rightarrow S_0$ transition boosted by strong spin-orbit coupling.[20]

(ii) TADF materials with Cu(I) and Pd(II) elements as well as those bearing earth-abundant metal elements may not serve as adequate blue emitters due to either the weakened metal–ligand interaction, slower reverse intersystem crossing, or the inability in obtaining high energy blue emission.[21–26]

(iii) Blue emissive Au(I) phosphors are unstable due to the inherent linear geometry with two *trans*-arranged monodentate ligands,[27] while the tetradentate Pt(II) or Au(III)-based phosphors may show good metal–chelate bond strength, but their performances may be hampered by the long radiative lifetime due to the reduced metal-to-ligand charge transfer (MLCT) or enhanced ligand-to-metal charge transfer (LMCT) contributions.[28–31]

Standing on basic chemical and photophysical theories, the Ir(III) carbene complexes possess strong metal-chelate bonding and shortened radiative lifetimes.[32–36] However, there is more room for improvement, especially from the aspect of molecular design. Herein, we present a new strategy for designing Ir(III) carbene blue phosphors, to which the electron transfer channel upon excitation is different from the traditional pathway. Scheme 1 depicted two such chelate designs; namely **L12H$_2$**$^+$ and **L13H$_2$**$^+$, whereas *peri*-CN substituted **L12** cyclometalate (Scheme 1a) is expected to show a typical electron transition process from the occupied π-orbitals of cyclometalating aryl group and Ir(III) metal center to the empty π-orbitals of the carbene entity, while the **L13**-associated Ir(III) complexes exhibited the transition from the similar origin but landed at the perpendicular arranged 4-cyanophenyl appendage of the carbene entity (vide infra, see Scheme 1b). We envision that the distinctive design of **chelate L13** may provide further understanding of the transition metal complexes showing the through-space charge transfer (TSCT) processes that are vital to many purely organic TADF emitters,[37–42] but rare in the metal phosphors. As a result, this modification, being facile, may lead to remarkable alternation in photophysical properties and OLED device performance. Standing on MLCT and TSCT processes of Ir(III) complexes, understanding of whether long-lived emission is phosphorescence or TADF, which is the current topic of greatest interest, is gained. Detailed results and discussion are elaborated as follows.

Results and Discussion

Synthesis and Characterization

As depicted in Scheme S1, the targeted pro-chelates **L12H$_2$**$^+$ and **L13H$_2$**$^+$ were synthesized from functional 2-fluoro-3-nitrobenzene derivatives, namely: 1-bromo-2-fluoro-3-nitrobenzene and 2-fluoro-1-methyl-3-nitrobenzene. Firstly, treatment of these compounds with 4-aminobenzonitrile in the presence of KOH at RT afforded 4-((2-bromo-6-nitrophenyl)amino)benzonitrile (**A**) and 4-((2-methyl-6-nitrophenyl)amino)benzonitrile (**B**). Then, a two-step in one-pot approach was applied to reduce the nitro group with iron powder, followed by cyclization in formic acid, giving the bromo- and methyl-substituted benzo[*d*]imidazoles (**C**) and (**D**). The bromo substituent in **C** was next converted to cyano substituent in 1-(4-cyanophenyl)-1*H*-benzo[*d*]imidazole-7-carbonitrile (**E**) using zinc cyanide and with Pd(PPh$_3$)$_4$ catalyst. Finally, the benzo[*d*]imidazolylidene pro-chelates **L12H$_2$**$^+$ and **L13H$_2$**$^+$ (cf., Scheme 1) were obtained using direct *N*-arylation of benzo[*d*]imidazoles **E** and **D** with (4-*tert*-butylphenyl)(mesityl)iodonium triflate in the presence of copper catalyst Cu(OAc)$_2$ upon heating.

Treatment of these carbene pro-chelates with *mer*-[IrCl$_3$(tht)$_3$] was next executed with an attempt to prepare the tris-bidentate Ir(III) carbene complexes using our synthetic protocols, i.e., NaOAc as a promoter in high boiling aromatic solvent.[43–45] Accordingly, these reactions have afforded two isomeric complexes, ***f*-ct12b,c** from chelate **L12H$_2$**$^+$ and ***f*-ct13b,c** from chelate **L13H$_2$**$^+$, in modest yields. Their structural drawings were depicted in Scheme 2, with cyclometalating modes revealed. Remarkably, their reaction patterns are in sharp contrast to that obtained from the analogous pro-chelate **L(CN1)H$_2$**$^+$,[46] possessing the same *peri*-cyano substituted benzo[*d*]imidazolylidene, but without the electron deficient *N*-4-cyanophenyl substituent. Its reaction with *mer*-[IrCl$_3$(tht)$_3$] had unequivocally yielded the

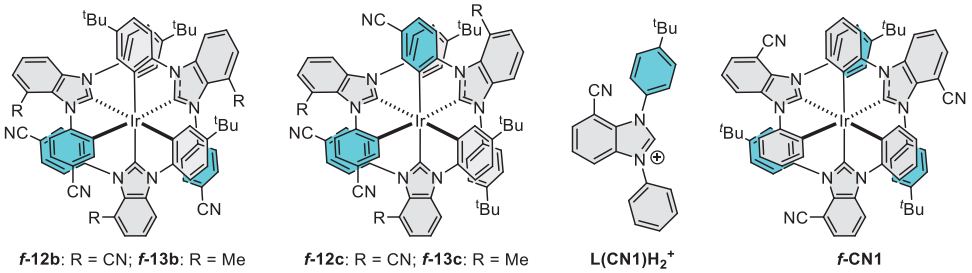

Scheme 2. Structural drawings of the studied Ir(III) complexes ***f*-ct12b,c** and ***f*-ct13b,c**, pro-chelate **L(CN1)H$_2^+$**, and homoleptic Ir(III) complex ***f*-CN1**.

symmetrical Ir(III) complex ***f*-CN1** as the sole product, to which its formation agreed with the steric influence imposed by the *peri*-cyano substituent. On the other hand, both pro-chelates **L12H$_2^+$** and **L13H$_2^+$** failed to give this symmetrical Ir(III) product, i.e., those denoted as "**a**" and "**d**" isomers according to our previous nomenclature,[47,48] but only the asymmetric products **b** and **c**. This new reaction pattern can be rationalized by the inclusion of electronic effects; that is, the electron-deficient cyclometalate is thermodynamically more stable and favorable to react,[49] and can overcome the steric blockage imposed by the *peri*-substituent. However, the insertion of too many of these electron-deficient cyclometalates may also reduce the reactivity of Ir(III) metal center and eventually prohibit further reaction, leaving an absence (or diminution) of isomer "**d**."

These complexes were further verified by high-resolution mass spectrometry, ^{1}H NMR spectroscopy, and elemental analyses. Their ^{1}H NMR spectra indicated possession of only the asymmetrical cyclometalates, which unambiguously ruled out the formation of symmetric Ir(III) complexes. Single crystal X-ray diffraction studies were next executed on Ir(III) metal complexes ***f*-ct12c** and ***f*-ct13b**,**c**, for which the refinement parameters and structural data are summarized in the Supporting Information, while the respective molecular drawings are depicted in Figures S1–S3. These structures are akin to the analogous Ir(III) carbene derivatives reported earlier,[50,51] confirming our structural identification.

Photophysical Properties

Their photophysical properties were evaluated, of which the absorption spectra recorded in toluene are depicted in Figure 1, while the corresponding numeric data are summarized in Table 1. As can be seen, both Ir(III) complexes ***f*-ct12b**,**c** exhibit a broad absorption band at 370 nm (***f*-ct12b**) and 365 nm (***f*-ct12c**), which is most plausibly attributed to the spin-allowed metal-to-ligand charge transfer (MLCT) transition in combination with intramolecular ligand-to-ligand charge transfer (LLCT) that occurs in common *fac*-arranged Ir(III) complexes with tris-bidentate carbene cyclometalates (vide infra). The 370 nm absorption of ***f*-ct12b** being further red-shifted in reference to that (365 nm) of ***f*-ct12c** can be rationalized by the reduced number of 4-cyanophenyl cyclometalate attached at the Ir(III) center, i.e., with reduced MLCT contribution. Alternatively, both ***f*-ct13b**,**c** exhibit

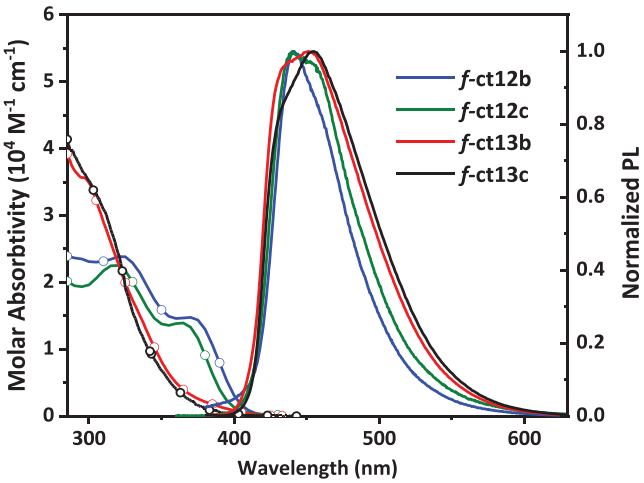

Figure 1. Absorption and emission spectra of studied Ir(III) complexes in toluene at 10–5 M at RT.

mainly the TSCT transition from the occupied orbitals (HOMO) of cyclometalating chelate to the 4-cyanophenyl appendage (LUMO), accompanied by a small contribution from the metal d_π-orbitals to 4-cyanophenyl appendage (see Computational Section, vide infra). The large spatial charge separation between cyclometalating chelate and 4-cyanophenyl appendage is expected to reduce the transition probability for ***f*-ct13b**,**c** (cf. ***f*-ct12b**,**c**), rendering lowered absorptivity in the lower-lying ($S_0 \rightarrow S_1$) electronic transition. Experimentally, this is supported by the absorption spectra of ***f*-ct13b** (Figure 1), where the absorption coefficient is $<< 5 \times 10^3$ M^{-1} cm^{-1} in the spectral region of >350 nm, much lower than that of $>10^4$ M^{-1} cm^{-1} for ***f*-ct12b,c**. Consequently, the different types of charge transfer pathways for both ***f*-ct12b,c** and ***f*-ct13b,c** are determined by the relative absorptivity in the lower-lying absorption band (350–400 nm), together with the computational approaches (vide infra). In brief, for ***f*-ct12b,c**, the main contribution for the lowest-lying transition is MLCT and LLCT, while it is dominated by TSCT for ***f*-ct13b,c**.

All Ir(III) complexes exhibited broadened emission bands together with little vibronic progression. This behavior differed from that of relevant *fac*-arranged Ir(III) carbene complexes documented in literature,[52–54] indicating an increased proportion of LLCT contribution at the excited states. Moreover, the emission profile of ***f*-ct12b**,**c** is slightly

Table 1: Photophysical data of relevant Ir(III) complexes recorded in toluene at RT.

	abs λ_{max} (nm)[a]	em λ_{max} (nm)[a]	FWHM (nm)[b]	PLQY (%)[c,d]	τ_{obs} (μs)[c]	τ_{rad} (μs)[c]	k_r (10^5 s^{-1})	k_{nr} (10^5 s^{-1})
***f*-ct12b**	320 (2.38), 370 (1.48)	442	53	80	1.90	2.38	4.2	1.1
***f*-ct12c**	318 (2.25), 365 (1.39)	440, 456 (sh)	62	76	2.25	2.96	3.4	1.1
***f*-ct13b**	298 (3.5)	435 (sh), 451	78	72	2.90	4.06	2.5	0.98
***f*-ct13c**	310 (3.1)	433 (sh), 455	80	60	6.22	10.3	0.97	0.64

[a] Recorded in degassed toluene at a conc. of 10^{-5} M at RT; extinction coefficient (ε) is given in parentheses with a unit of 10^4 $M^{-1}\cdot cm^{-1}$. [b] Full width at half maximum. [c] Recorded in degassed toluene at a conc. of 10^{-5} M and with excitation at 365 nm. [d] Coumarin 102 (C102) in methanol (PLQY = 87% and λ_{max} = 480 nm) was employed as standard.

blue-shifted and underwent a decrease in bandwidth in reference to the derivatives ***f*-ct13b**,**c**. Obviously, both observations are caused by the cyano-to-methyl conversion at the *peri*-position of benzo[*d*]imidazolylidene fragment. The radiative (k_r) and nonradiative (k_{nr}) transition rate constants were also deduced from their quantum yield (PLQY) and observed lifetime (τ_{obs}) data using the following equations. $k_r = PLQY/\tau_{obs}$ and $k_{nr} = (1 - PLQY)/\tau_{obs}$. All pertinent data are listed in Table 1. Careful examination indicates that ***f*-ct12b** exhibited relatively larger radiative decay rate constants (k_r) than ***f*-ct12c**, being 4.2 and 3.4 × 10^5 s^{-1}, respectively. This suggests that increasing number of cyanophenyl cyclometalate from **b** to **c** reduces k_r due to the reduction of electron density at the Ir(III) center and MLCT contribution (vide supra). On the other hand, the radiative decay rate constant for ***f*-ct13b** and ***f*-ct13c** is deduced to be 2.5 × 10^5 and 0.97 × 10^5 s^{-1}, respectively. In comparison to ***f*-ct12b,c,** the trend of smaller k_r values for ***f*-ct13b,c**, qualitatively seems to correlate well with the absorption spectra, where the large TSCT contribution in ***f*-ct13b,c** reduces the transition dipole moment and hence the decrease of k_r value. More quantitative and in-depth discussion will be presented in the following section of theoretical approach.

Theoretical Approach

Further insights into the photophysics were comprehended by conducting time-dependent (TD)-DFT calculations,[55–57] where we explored the lowest singlet (S_1) and triplet (T_1) excited states of the studied Ir(III) complexes (***f*-ct12b**,**c** and ***f*-ct13b**,**c**) in toluene solution (B3LYP-D3(BJ)/def2-SVP level with PCM for toluene). As a result, the vertical excitation energies of the $S_0 \rightarrow T_1$ transition were 439 and 437 nm for ***f*-ct12b**,**c**, and 448 and 431 nm for ***f*-ct13b**,**c**, respectively (Table 2). These values were comparable to the experimental emission λ_{max} at 442, 440, 451, and 455 nm shown in Figure 1 and Table 1, where the mean absolute deviation (MAD) between experimental and calculated results was about 0.05 eV (or 1.2 kcal mol^{-1}). For the $S_0 \rightarrow S_1$ transition, the vertical excitation energies (416 and 403 nm) of ***f*-ct12b**,**c** closely align with the experimental absorption onset at ~405 nm (Figure 1). In addition, for ***f*-ct13b**,**c**, the $S_0 \rightarrow S_1$ vertical excitation (446 and 426 nm) is slightly offset from their absorption onset at ~400 nm. Furthermore, the calculated oscillator strengths of ($S_0 \rightarrow S_1$) transition for ***f*-ct13b**,**c** (i.e., 0.0034 and 0.0008) are much smaller than those of ***f*-ct12b**,**c** (i.e., 0.0210 and 0.0379). This result suggests

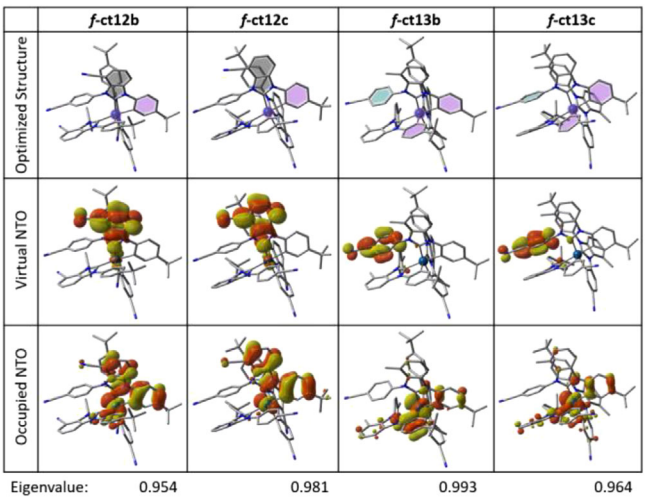

Figure 2. The first row depicted the optimized ground state structure with the main donor, acceptor, and overlapped donor–acceptor π-orbitals highlighted in pink, green, and grey; while the second and third rows showed the virtual and occupied NTO pairs for the respective $S_0 \rightarrow T_1$ transition of ***f*-ct12b**,**c** and ***f*-ct13b**,**c** (at optimized S_0 structures).

distinctive transition characteristics between ***f*-ct12b**,**c** and ***f*-ct13b**,**c**, which align well with the much weaker $S_0 \rightarrow S_1$ absorption coefficient of ***f*-ct13b**,**c** observed experimentally.

To better understand their $S_0 \rightarrow T_1$ transitions, natural transition orbital (NTO) analysis,[58] which can illustrate the transition using a pair of orbitals, was also performed, and the NTO pairs are shown in Figure 2. For ***f*-ct12b**,**c**, where the occupied NTOs are localized over both the ligands (in π orbitals) and the Ir(III) atom, while the virtual NTOs are primarily localized over the cyclometalating carbene fragments (in the π^* orbitals). These results suggest that the $S_0 \rightarrow T_1$ transition of ***f*-ct12b**,**c** is mainly attributed to MLCT. In sharp contrast, for ***f*-ct13b**,**c**, the occupied NTOs are localized on the cyclometalating chelate and the Ir(III) atom, while the virtual NTOs were notably localized on the *N*-substituted 4-cyanophenyl appendage. To gain further insights, we then performed the relevant molecular orbital (MO) contributions of selected electronic transitions via the inter-fragment charge transfer (IFCT) analysis of the $S_0 \rightarrow T_1$ transitions for ***f*-ct12b**,**c** and ***f*-ct13b**,**c** using Multiwfn software package.[59]

The results, which include contributions (in %) from TSCT, MLCT, LMCT, LLCT, ligand-centered (LC), and metal-centered (MC), are listed in Table 2. Detailed definitions of individual transition characters are provided in

Table 2: TD-DFT calculation data and molecular orbital (MO) contributions (>15%) of the $S_0 \rightarrow S_1$ and $S_0 \rightarrow T_1$ excitations, and $S_0 \rightarrow T_1$ excitation charge character assignments of ***f*-ct12b,c** and ***f*-ct13b,c** optimized structures.

	E_{HOMO}/E_{LUMO} (eV)[a]	Excitation	λ (nm)/ (eV)[b]	f[b]	ΔE_{ST} (eV/kcal mol^{-1})	MO Contribution (>15%)[b]	Assignment[c] TSCT	MLCT	LMCT	LLCT	LC	MC
***f*-ct12b**	–5.74/–2.23	$S_0 \rightarrow T_1$	439/2.82	0	0.16/3.7	HOMO → LUMO + 1 (39.0%) HOMO → LUMO (18.5%) HOMO → LUMO + 2 (16.0%)	4.4%	21.8%	2.7%	46.6%	23.6%	0.9%
		$S_0 \rightarrow S_1$	416/2.98	0.0210		HOMO → LUMO (94.0%)						
***f*-ct12c**	–5.83/–2.20	$S_0 \rightarrow T_1$	437/2.84	0	0.24/5.5	HOMO → LUMO + 2 (37.0%) HOMO → LUMO + 1 (22.1%) HOMO → LUMO (15.1%)	2.5%	15.9%	2.8%	42.7%	35.5%	0.6%
		$S_0 \rightarrow S_1$	403/3.08	0.0379		HOMO → LUMO (75.5%)						
***f*-ct13b**	–5.41/–2.09	$S_0 \rightarrow T_1$	448/2.76	0	0.02/0.46	HOMO → LUMO (93.8%)	78.7%	4.4%	0.5%	14.5%	1.6%	0.3%
		$S_0 \rightarrow S_1$	446/2.78	0.0034		HOMO → LUMO (97.6%)						
***f*-ct13c**	–5.51/–2.07	$S_0 \rightarrow T_1$	431/2.88	0	0.03/0.69	HOMO → LUMO (85.0%)	68.6%	7.2%	0.8%	19.3%	3.6%	0.4%
		$S_0 \rightarrow S_1$	426/2.91	0.0008		HOMO → LUMO (96.5%)						

[a] The E_{HOMO} and E_{LUMO} of optimized S_0 structures in toluene calculated at B3LYP-D3(BJ)/def2-SVP level with polarizable continuum model (PCM). [b] The vertical excitation energy (λ), oscillator strength (f), and MO contribution obtained by TD-DFT method at B3LYP-D3(BJ)/def2-SVP level with PCM for toluene. [c] The assignments studied by IFCT (Hirshfeld) method at optimized S_0 structures.

the Supporting Information (SI). For ***f*-ct12b,c**, it was found that the MLCT character decreased from 21.8% (***f*-ct12b**) to 15.9% (***f*-ct12c**), a reduction of about 5.9% as the number of 4-cyanophenyl cyclometalates attached to the iridium atom increased (Table 2). This decrease in MLCT percentages corresponds well with the reduced experimental k_r values (in 10^5 s^{-1}, Table 1), from 4.2 (***f*-ct12b**) to 3.4 (***f*-ct12c**). In the case of ***f*-ct13b,c**, the MLCT contributions were significantly reduced to minimal values (4.4% and 7.2%, respectively) compared to ***f*-ct12b,c**. The dominant characters in the $S_0 \rightarrow T_1$ excitation of ***f*-ct13b,c** are TSCT (78.7% for ***f*-ct13b** and 68.6% for ***f*-ct13c**). Instead of MLCT contribution, the dominated TSCT contributions in the ***f*-ct13b,c** should be a better representation of their actual $S_0 \rightarrow T_1$ transition behavior. The decrease in the TSCT contribution from 78.7% (***f*-ct13b**) to 68.6% (***f*-ct13c**) also corresponds well with the decrease of k_r from ***f*-ct13b** (2.5×10^5 s^{-1}, Table 1) to ***f*-ct12c** (0.97×10^5 s^{-1}) deduced experimentally. This positive correlation between TSCT contribution and k_r values for isomeric compounds has been reported in previous theoretical studies on fluorescence molecules.[42,60–65] Our IFCT results for ***f*-ct12b,c** and ***f*-ct13b,c** also suggest that MLCT transition is more efficient than TSCT transition, where a larger MLCT percentage (~20% in ***f*-ct12b,c**) is associated with a larger k_r value, while a high TSCT percentage (~70% in ***f*-ct13b,c**) correlates with a relatively lowered k_r value.

The emission radiative lifetime (τ_{rad}) and rate constant (k_r) calculations were also conducted theoretically. Although it was anticipated that there would be sufficient time for many of these studied Ir(III) complexes to transform into lower-energy structures from the excited T_1 state since the lifetime of phosphorescence is believed to be relatively long, the emitting structure was expected to be an intermediate between the T_1 and S_0 states.[66–69] Many reported works suggested both the T_1 and S_0 optimized structures might provide predictions matching the experimental results.[66–68] Consequently, both the optimized S_0 and T_1 structures were used to study the τ_{rad} and k_r with spin-orbit coupling (SOC)-TDDFT method and the calculation results of their arithmetic and Boltzmann average are summarized in Table 3. Herein, we only discuss the arithmetic average for simplicity. The calculated τ_{rad} of ***f*-ct12b** ($T_1 \rightarrow S_0$ emission) was 0.64 μs (at the S_0 structure) and 1.26 μs (at the T_1 structure). Compared to the experimental τ_{rad} (2.38 μs, Table 1), the theoretical τ_{rad} values for their S_0 and T_1 structures were slightly smaller. For ***f*-ct12c**, the experimental τ_{rad} of 2.96 μs lies between the theoretical τ_{rad} of 1.14 μs (at the S_0 structure) and 4.67 μs (at the T_1 structure). For ***f*-ct13b**, the calculated τ_{rad} of 6.94 μs (at the S_0 structure) and 7.28 μs (at the T_1 structure) are both larger than its experimental τ_{rad} of 4.06 μs, while the experimental τ_{rad} of ***f*-ct13c** (10.3 μs) falls between the two calculated values of 3.88 μs (at the S_0 structure) and 16.8 μs (at the T_1 structure). This trend resembles that derived experimentally.

Phosphorescence Versus Thermally Activated Delayed Fluorescence

The abovementioned calculation appears to be qualitatively consistent with experimental absorption ($S_0 \rightarrow S_1$) and emission data ($T_1 \rightarrow S_0$). However, on a wider basis, we must consider other possibilities for the T_1-associated emission kinetics. As shown in Table 2, the energy gap between S_1 and T_1 states, i.e., ΔE_{ST}, is estimated to be 3.7 and 5.5 kcal mol^{-1} for ***f*-ct12b,c**, respectively. The large ΔE_{ST} of ***f*-ct12b,c** is due to the increased contribution of LLCT and MLCT to the S_1 and T_1 states, where electron correlation energy is large. On the other hand, ΔE_{ST} is calculated to be as small as 0.46 and 0.69 kcal mol^{-1} for ***f*-ct13b,c**, respectively. These smaller ΔE_{ST} can be rationalized by the dominant TSCT character, where the spatially separated charge transfer process weakens the electron correlation energy, which, theoretically, allows reverse intersystem crossing (RISC)

Table 3: Predicted adiabatic and vertical emission energy of $T_1 \rightarrow S_0$ transition, emission radiative lifetime (τ_{rad}), and radiative rate constant (k_r) calculated for ***f*-ct12b**,**c** and ***f*-ct13b**,**c**.

Emission ($T_1 \rightarrow S_0$)	λ (nm)/(eV)[a]	λ (nm)/(eV)[b]	τ_{rad} (μs)[c]	k_r (μs^{-1})[c]
***f*-ct12b**	444/2.79	445/2.79 (***463/2.68***)	0.64/0.72 (***1.26/1.33***)	1.57/1.38 (***0.79/0.75***)
***f*-ct12c**	446/2.78	442/2.81 (***552/2.25***)	1.14/1.25 (***4.67/4.84***)	0.88/0.80 (***0.21/0.21***)
***f*-ct13b**	447/2.83	454/2.73 (***513/2.42***)	6.94/6.93 (***7.28/7.15***)	0.14/0.14 (***0.14/0.14***)
***f*-ct13c**	448/2.85	436/2.84 (***554/2.24***)	3.88/3.87 (***16.8/16.9***)	0.26/0.26 (***0.06/0.06***)

[a] Adiabatic emission energy of T_1 and S_0 optimized structures in toluene calculated at B3LYP-D3(BJ)/def2-SVP level with PCM. [b] Vertical SOC-TDDFT emission energy between T_1 and S_0 states of S_0 (normal font) and T_1 (italic and bold font in parentheses) optimized structures. [c] Data of τ_{rad} and k_r were the computed arithmetic average/Boltzmann average (298 K) of the SOC sub-states with S_0 (normal font) and T_1 (italic and bold font in parentheses) optimized structures.

at RT, fulfilling the necessary condition for TADF.[37–42] Therefore, while the long-lived emission of ***f*-ct12b,c** can be unambiguously ascribed to phosphorescence, it is of great interest to probe the origin of long-lived emission of ***f*-ct13b**,**c** to be either phosphorescence or TADF. This issue is of great importance from both fundamental and application aspects. Recently, it has been proposed that by combining strong spin-orbit coupling and thermally accessible ΔE_{ST}, RISC rate can be enhanced drastically; consequently, the delayed lifetime of TADF may be reduced to a time scale much shorter than micro- to milliseconds limited for traditional TADF processes.[70–72] Transition metal complexes are ideal candidates in confirming this concept. Of particular interest are the Ir(III) complexes due to both the stronger metal–ligand interaction and heavy-atom effect. Evidently, ***f*-ct13b** (or **c**) provides an exquisite prototype for the corresponding temperature-dependent time-resolved emission measurement. In this study, to maintain the same viscosity and phase throughout a wide temperature range, the experiment was carried out for ***f*-ct13b** in solid state, where multichannel scaling (MCS) measurements were conducted from 10 to 300 K (see Figure S4 in SI), with the data fitted by a bi-exponential decay function. One of the decay components was found to be strongly temperature dependent. In contrast, the other decay component remained nearly unchanged across the studied temperatures, which can be attributed to the defect relaxation in the solid state. We then plot the emission lifetime against temperature shown in Figure 3. The plot can thus be fitted by Equation (1) expressed below:[73,74]

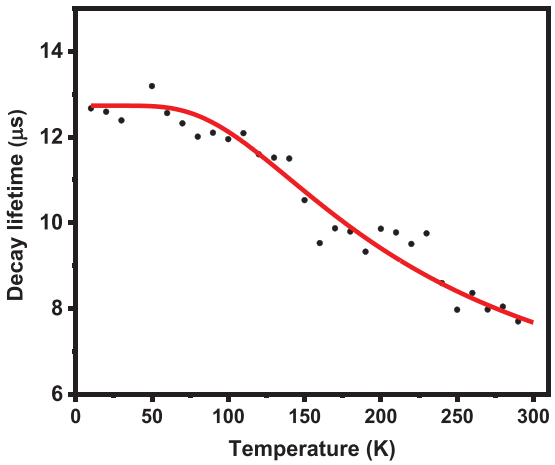

Figure 3. Plot of temperature-dependent decay lifetime of ***f*-ct13b** powder as a function of temperature between 10 and 300 K (red solid line). The fitting is conducted using Equation (1) (see text for detail).

$$\tau(T) = \frac{1 + \exp\left(-\frac{\Delta E(II-I)}{k_B T}\right) + \exp\left(-\frac{\Delta E(III-I)}{k_B T}\right) + \exp\left(-\frac{\Delta E(S_1-I)}{k_B T}\right)}{\frac{1}{\tau(I)} + \frac{1}{\tau(II)}\exp\left(-\frac{\Delta E(II-I)}{k_B T}\right) + \frac{1}{\tau(III)}\exp\left(-\frac{\Delta E(III-I)}{k_B T}\right) + \frac{1}{\tau(S_1)}\exp\left(-\frac{\Delta E(S_1-I)}{k_B T}\right)} \quad (1)$$

where τ(I), τ(II), and τ(III) are the lifetimes of triplet substates I, II, and III, respectively; ΔE(II–I) and ΔE(III–I) are the energy gaps between substates II and I, and substates III and I, respectively. However, the lowest temperature applied in the study is 10 K, where three triplet sublevels can be treated as degenerated. Therefore, ΔE and τ are assumed to be the same for all three triplet sublevels in Equation (1); while k_B is the Boltzmann constant. Equation (1) is usually applied to determine the contribution of TADF.[75] The better the fitting, the higher the percentage of emissions that originate from TADF rather than phosphorescence, which is particularly popular in recent debate regarding phosphorescence or TADF in the transition metal complexes with small ΔE_{ST}.[75–78]

Using Equation (1), the best fit with estimated standard deviation (ESD) > 0.98 in Figure 3 seems to provide evidence for the contribution of TADF for ***f*-ct13b**. Furthermore, extrapolation of the decay lifetimes for the triplet state of ***f*-ct13b** at 300 K using Equation (1) gives a lifetime of 7.0 μs and a ΔE_{ST} of ~0.03 eV (0.69 kcal mol^{-1}), which is consistent with 0.46 kcal mol^{-1} derived from computational approach. Based on the fitting results of Equation (1), the contribution of TADF and phosphorescence for ***f*-ct13b** can be calculated

by Equation (S1) at each temperature (see SI), and the results are shown in Figure S5 (also see SI). As a result, for ***f*-ct13b**, the TADF contribution reaches roughly 50% at RT, which provides additional evidence to support small ΔE_{ST} and its emission kinetics to be associated with both TADF and phosphorescence. Yet, in another approach, the S_1–T_1 spin-orbit coupling constant for ***f*-ct13b** is calculated to be as high as 35.46 cm^{-1}. Therefore, the rates of ISC and RISC should be much faster than the decay rate constants of both fluorescence and phosphorescence. Thus, kinetically, there is an existence of pre-equilibrium between the S_1 and T_1 states such that both phosphorescence and TADF experience the same decay lifetime. This, combined with the ultrafast rates of ISC and RISC (~0 for ΔE_{ST} in ***f*-ct13b**), makes differentiation of phosphorescence and TADF virtually impossible. For the same reason, its experimental ΔE_{ST} cannot be determined by simply separating the fluorescence and phosphorescence. In other words, the broadened emission observed in ***f*-ct13b** is attributed to the superposition of TADF and phosphorescence. This result thus highlights the difficulty in differentiating phosphorescence and TADF in ***f*-ct13b**. We also believe that for all Ir(III) complexes with ΔE_{ST}~0 and strong spin-orbit coupling, it may be of little opportunity to spectroscopically explore whether the observed emission is phosphorescence or TADF at ambient temperature.

Thermal and Electrochemical Properties

Thermal and electrochemical properties are necessary information for fabrication of OLEDs. Thermogravimetric (TG) analysis indicated the existence of a slightly lowered T_d of 388 °C for ***f*-ct12b** and T_d of >427 °C for the rest of Ir(III) complexes, to which T_d was gauged by the temperature showing a weight loss of 5% (Figure S6). Moreover, ***f*-ct13b**,**c** can be sublimed without decomposition, but ***f*-ct12b**,**c** underwent decomposition during vacuum sublimation. This could be due to the existence of six cyano groups, which increased the intermolecular nonbonding interaction and severely limited the volatility. Next, their redox potentials were recorded using cyclic voltammetry (CV) in acetonitrile. As shown in Figure S7, Ir(III) complexes ***f*-ct12b**,**c** exhibited reversible reduction bands, while that of ***f*-ct13b**,**c** turned irreversibly due to the removal of three cyano groups on complexes. Moreover, ***f*-ct12b**,**c** and ***f*-ct13b**,**c** exhibited reversible oxidation peaks at 0.69, 0.81, 0.52, and 0.60 V, respectively. These bands were assigned to the oxidation that occurred at the Ir(III) metal center, to which the potentials of ***f*-ct12b**,**c** are more anodic shifted in comparison to those of ***f*-ct13b**,**c** due to the presence of three *peri*-cyano substituents, while both the isomers "**c**" with two cyanophenyl cyclometalates were found to be stabilized by ~0.10 V compared to their analogue "**b**," each with only one cyanophenyl cyclometalate. Finally, their oxidation onsets were employed to calculate the HOMOs, taking ferrocene as the reference. Next, their LUMO levels were estimated using the experimentally obtained optical gap and associated HOMO data. These parameters were listed in Table 4, as they are important parameters for designing the OLED devices.

Table 4: Voltammetric data, experimental energy gaps, and decomposition temperature (T_d) of the studied Ir(III) complexes at RT.

Complex	$E_{ox,\ onset}$ (eV)[a]	E_{HOMO} (eV)[b]	E_g^{opt} (eV)[c]	E_{LUMO} (eV)[d]	T_d (°C)[e]
***f*-ct12b**	0.69	–5.48	2.99	–2.49	388
***f*-ct12c**	0.81	–5.61	3.00	–2.61	465
***f*-ct13b**	0.52	–5.32	3.02	–2.30	427
***f*-ct13c**	0.60	–5.40	3.01	–2.39	449

[a] Electrochemical potentials were measured in a 0.1 M acetonitrile solution of $TBAPF_6$. referenced to the Fc/Fc^+ couple; E_{ox} onset is the onset potential for the oxidation wave. [b] HOMO = $-(E_{ox}$ onset + 4.8). [c] Energy gap = 1240/[PL_{onset} (nm)]. [d] LUMO = HOMO + energy gap. [e] Temperature with a 5% loss in weight.

Device Fabrication and Characterization

For probing potential applications, the TSCT phosphor ***f*-ct13b** was first selected as the dopant and sensitizer in fabrication of OLED and hyper-OLED devices due to its high synthetic yield, promising photophysical properties, and good volatility. Next, OLEDs were fabricated in a multi-layered architecture: ITO/(HATCN, 5 nm)/(TAPC, 30 nm)/(TCTA, 15 nm)/(mCBP, 10 nm)/(EML, 25 nm)/(PPF, 10 nm)/(ANT-BIZ, 30 nm)/Liq (2 nm)/Al (100 nm), to which 2,8-bis(diphenylphosphoryl)dibenzo[*b*,*d*]furan (PPF) and 1,4,5,8,9,11-hexaazatriphenylenehexacarbonitrile (HATCN) were employed as the high triplet-energy host material in the emissive layer (EML) and hole injection layer, respectively. Both 4,4′-cyclohexylidenebis[*N*,*N*-bis(4-methylphenyl)benzenamine] (TAPC) and 4,4′,4″-tris(carbazol-9-yl)triphenylamine (TCTA) served as the hole transporting layers, and 1-[4-(10-([1,1-biphenyl]-4-yl)anthracen-9-yl)phenyl]-2-ethyl-1*H*-benzo[*d*]imidazole (ANT-BIZ) as the electron transporting layer. Finally, 3,3′-di(9*H*-carbazol-9-yl)-1,1′-biphenyl (mCBP) and PPF functioned as the electron and hole blocking layers, respectively. The energy level diagram and molecular structures of employed organic materials are depicted in Figures S8 and S9.

Figure S10 and Table 5 depicted the device characteristics of OLED based on ***f*-ct13b** with varied doping concentrations. Interestingly, the EL profiles displayed nearly no concentration dependence with broad emission band centered at ~453 nm. To identify the nature of emission, the photoluminescence of 30 wt% of ***f*-ct13b** doped in PPF host was measured, affirming the well confinement of excitons within the EML (Figure S11 and Table S2).

Notably, ***f*-ct13b** possesses a relatively shallow HOMO energy level (–5.32 eV) than that of the PPF host (–6.7 eV), leading to possible hole trapping in this system. It has been reported that higher ratio of dopant could facilitate the hole-transporting property within the EML.[79] As predicted, we observed that, within this series of OLED devices, the increased doping ratio of ***f*-ct13b** has greatly improved the device performances in terms of both the current density and EQE. Additionally, the driving voltages at 100 cd m^{-2} were also reduced from 5.2 to 4.4 V, indicating more balanced carrier transport at higher doping concentrations.

Table 5: Phosphorescent and hyper-OLED devices using TSCT phosphors and *ν*-DABNA terminal emitter co-deposited in PPF host material.

Emitter	Concentration (wt%)	*V* (V)[a]	CE (cd/A)[b]	EQE (%)[b]	CIE (*x*, *y*)[c]	λ_{EL} (nm)[c]	FWHM (nm)[c]
***f*-ct13b**	5%	3.6/5.2	10.4/6.4	10.0/6.3	(0.153, 0.117)	451	64
	13%	3.6/4.8	18.1/13.2	17.5/12.8	(0.154, 0.118)	452	64
	20%	3.6/4.4	21.3/18.5	21.3/18.5	(0.154, 0.119)	453	63
	30%	3.2/4.4	24.0/21.3	22.2/19.7	(0.155, 0.120)	455	64
***f*-ct13c**	30%	3.2/4.0	21.8/18.7	15.8/14.2	(0.164, 0.160)	456	74
ν-DABNA	1%	3.6/5.2	20.9/10.7	23.8/12.6	(0.118, 0.114)	471	19
	1% (w/***f*-ct13b**)	3.6/4.8	23.8/19.9	25.9/21.7	(0.121, 0.122)	471	19
	1% (w/***f*-ct13c**)	3.2/4.0	27.6/26.4	28.2/27.0	(0.123, 0.129)	472	20

[a] Data recorded at 1 and 100 cd m^{-2}. [b] Corresponding maximum value and data that recorded at 100 cd m^{-2}. [c] Data measured at 100 cd m^{-2}.

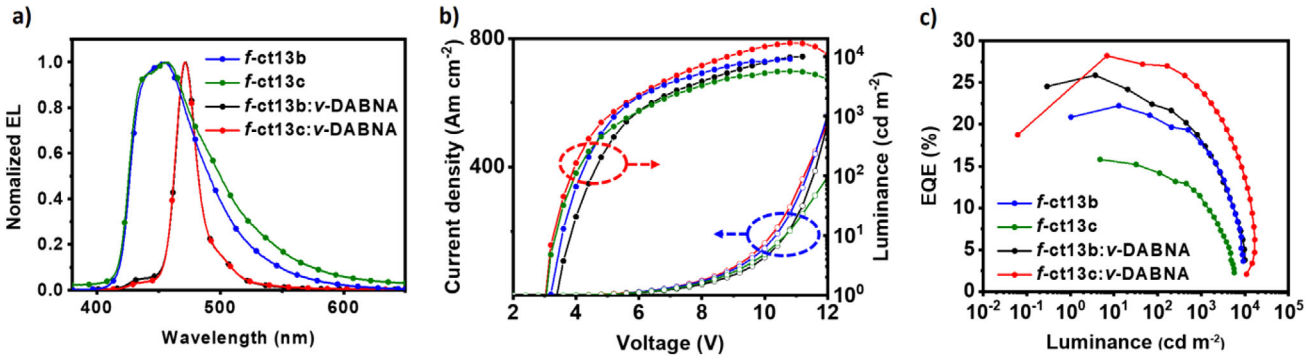

Figure 4. OLED performances based on TSCT phosphors ***f*-ct13b** and ***f*-ct13c** at doping ratios of 30 wt% in PPF. a) EL spectra; b) current density–voltage–luminance (*J*–*V*–*L*) curves; and c) external quantum efficiency (EQE) versus luminance.

Furthermore, as shown in Figure S12, the device with 30 wt% of ***f*-ct13b** showed no variation in terms of peak position and spectral profile upon increasing the driving voltage, affirming its high performance. Finally, as shown in Figure 4, our study was further extended to ***f*-ct13c** and with its performances also recorded at 30 wt%. Overall, max. EQEs of 22.2% and 15.8%, together with max. luminance of 9127 and 5687 cd m^{-2} were documented for devices with ***f*-ct13b,c**, respectively.

Recently, multiple resonance thermally activated delayed fluorescence (MR-TADF) emitters have gained significant popularity due to their unique spectral properties and excellent performances.[10,80–82] Relevant emitters feature HOMO and LUMO localized on neighboring atoms, resulting in a narrowband emission, small Stokes shift, and high luminescence efficiency. Subsequently, emphasis was then shifted to TADF emitters or transition-metal phosphor-sensitized hyper-OLED devices.[13,46,83–85] In these systems, the sensitizers transferred their excitation energy to terminal MR-TADF emitters via efficient FRET, affording both high performances and color chromaticity. With the aim of realizing narrowband blue hyperphosphorescence, ***f*-ct13b** and ***f*-ct13c** were employed as the dopant sensitizer to convey their energy to the terminal emitter *ν*-DABNA. First, we co-doped our TSCT phosphors (30 wt%) and *ν*-DABNA (1 wt%) into the EML with PPF host. The resulting hyper-OLEDs displayed a nearly identical EL profile to that of the reference device with solely the terminal emitter *ν*-DABNA, affirming the efficient energy transfer (Figure 4). In addition to the improved color purity (FWHM = 18 nm), the ***f*-ct13b**-based hyper-OLED device exhibited max. EQE of 25.9% and max. luminance of approaching 10 000 cd m^{-2}. Upon switching to the second sensitizer ***f*-ct13c**, the recorded max. EQE was further boosted to 28.2%, together with an impressive max. luminance of 16 850 cd m^{-2}. Moreover, the phosphor ***f*-ct13c** also displayed further suppressed roll-off and improved EQE to 27.0% at 100 cd m^{-2}. Such high performances can be attributed to the efficient FRET facilitated by the relatively long radiative lifetime of ***f*-ct13c**, to which notable improvements in efficiencies for organic TADF emitters with long emission lifetimes were also demonstrated.[86]

Conclusion

In summary, we have designed and synthesized a new family of Ir(III) carbene complexes, i.e., *f*-ct12b,c and *f*-ct13b,c, which, respectively, showed the dominant MLCT and TSCT processes at the excited states. In fact, this system demonstrated, for the first time, the diminished MLCT but enhanced TSCT process in the Ir(III) metal emitters, i.e., *f*-ct13b,c. On the other hand, TSCT had only been observed in redox-inactive metal complexes and those with notably reduced heavy-atom effects. Hence, their photophysical properties were greatly affected by the transitions involving the inter- and intra-ligand charge transfer and noncovalent interactions.[21–26] Moreover, in contrast to the formation of all four possible Ir(III) complexes "a–d" from the asymmetric di-*N*-aryl carbene pro-chelates,[47,48,87] the absence of symmetric Ir(III) carbene isomers "a" and "d" during the formation of asymmetric products "b" and "c"

well illustrated the selectivity that exerted by the electron-deficient *N*-substituted 4-cyanophenyl appendage on the carbene cyclometalates. Thirdly, our photophysical measurement and theoretical calculations suggested that the MLCT process is more efficient than TSCT process in inducing the intersystem crossing, enabling slightly larger k_r values and giving shorter radiative lifetimes among the demonstrated Ir(III) complexes. Nevertheless, this work provides a new strategy in exploring the possible co-existence of TADF and phosphorescence in the Ir(III)-based complexes, which is recently a hot but debatable issue. Last but not least, the vacuum-deposited OLED devices with *f*-ct13b (30 wt%) as dopant in PPF delivered a blue emission peaking at 455 nm with max. EQE of 22.2%. Also, hyper-OLED bearing sensitizer *f*-ct13c and terminal emitter *ν*-DABNA afforded narrowband blue emission with FWHM of 20 nm and max. EQE up to 28.2%, demonstrating the great potential of such TSCT enhanced Ir(III) phosphors in future OLED applications.

Supporting Information

Details of chelate syntheses, single crystal X-ray diffraction analyses, supportive photophysical and electrochemical data, general statement of computational studies, TD-DFT results and transient decay experiments, supportive OLED performance data involving Ir(III) phosphor, and ^{1}H NMR spectra of all reported Ir(III) complexes.

Acknowledgements

Funding is provided by the University Grants Council of Hong Kong (CityU 11304221 and CityU 11312722) to Y.C., and National Natural Science Foundation of China (52130308) and Shenzhen Science and Technology Program (JCYJ 20220818095816036 and ZDSYS 20210623091813040) to C.Y., and National Science and Technology Council of Taiwan (NSTC 112-2639-M-002-007-ASP) and National Taiwan University to P.-T.C. The theoretical studies were carried out using the computing facility, i.e., CityU Burgundy at City University of Hong Kong.

Conflict of Interests

The authors declare no conflict of interest.

Data Availability Statement

The data that support the findings of this study are available in the Supporting Information of this article.

Keywords: Hyperphosphorescence · Organic light emitting diode · Phosphorescence · Space confined charge transfer · Thermally activated delayed fluorescence

[1] L. Xiao, Z. Chen, B. Qu, J. Luo, S. Kong, Q. Gong, J. Kido, *Adv. Mater.* **2011**, *23*, 926–952.
[2] H. Fu, Y.-M. Cheng, P.-T. Chou, Y. Chi, *Mater. Today* **2011**, *14*, 472–479.
[3] M. Zhu, C. Yang, *Chem. Soc. Rev.* **2013**, *42*, 4963–4976.
[4] X. Yang, X. Xu, G. Zhou, *J. Mater. Chem. C* **2015**, *3*, 913–944.
[5] Z. Xu, B. Z. Tang, Y. Wang, D. Ma, *J. Mater. Chem. C* **2020**, *8*, 2614–2642.
[6] D. Wang, C. Cheng, T. Tsuboi, Q. Zhang, *CCS Chem.* **2020**, *2*, 1278–1296.
[7] R. Czerwieniec, M. J. Leitl, H. H. H. Homeier, H. Yersin, *Coord. Chem. Rev.* **2016**, *325*, 2–28.
[8] H. Yersin, A. F. Rausch, R. Czerwieniec, T. Hofbeck, T. Fischer, *Coord. Chem. Rev.* **2011**, *255*, 2622–2652.
[9] P.-T. Chou, Y. Chi, M.-W. Chung, C.-C. Lin, *Coord. Chem. Rev.* **2011**, *255*, 2653–2665.
[10] Y. Kondo, K. Yoshiura, S. Kitera, H. Nishi, S. Oda, H. Gotoh, Y. Sasada, M. Yanai, T. Hatakeyama, *Nat. Photonics* **2019**, *13*, 678–682.
[11] M. Mamada, M. Hayakawa, J. Ochi, T. Hatakeyama, *Chem. Soc. Rev.* **2024**, *53*, 1624–1692.
[12] D. H. Ahn, S. W. Kim, H. Lee, I. J. Ko, D. Karthik, J. Y. Lee, J. H. Kwon, *Nat. Photonics* **2019**, *13*, 540–546.
[13] C.-Y. Chan, M. Tanaka, Y.-T. Lee, Y.-W. Wong, H. Nakanotani, T. Hatakeyama, C. Adachi, *Nat. Photonics* **2021**, *15*, 203–207.
[14] T. Fleetham, G. Li, J. Li, *Adv. Mater.* **2017**, *29*, 1601861.
[15] J. Sun, H. Ahn, S. Kang, S.-B. Ko, D. Song, H. A. Um, S. Kim, Y. Lee, P. Jeon, S.-H. Hwang, Y. You, C. Chu, S. Kim, *Nat. Photonics* **2022**, *16*, 212–218.
[16] E. Kim, J. Park, M. Jun, H. Shin, J. Baek, T. Kim, S. Kim, J. Lee, H. Ahn, J. Sun, S.-B. Ko, S.-H. Hwang, J. Y. Lee, C. Chu, S. Kim, *Sci. Adv.* **2022**, *8*, eabq1641.
[17] M. Jung, K. H. Lee, J. Y. Lee, T. Kim, *Mater. Horiz.* **2020**, *7*, 559–565.
[18] S. Diesing, L. Zhang, E. Zysman-Colman, I. D. W. Samuel, *Nature* **2024**, *627*, 747–753.
[19] Y. Wu, M. Huang, L. Cheng, J. Zhang, Y. Pan, S.-M. Yiu, K. C. Lau, J. Yan, C. Yang, Y. Chi, *Angew. Chem. Int. Ed.* **2025**, *64*, e202421664.
[20] M. A. Baldo, M. E. Thompson, S. R. Forrest, *Nature* **2000**, *403*, 750–753.
[21] R. Hamze, J. L. Peltier, D. Sylvinson, M. Jung, J. Cardenas, R. Haiges, M. Soleilhavoup, R. Jazzar, P. I. Djurovich, G. Bertrand, M. E. Thompson, *Science* **2019**, *363*, 601–606.
[22] W.-P. To, Q. Wan, G. S. M. Tong, C.-M. Che, *Trends Chem.* **2020**, *2*, 796–812.
[23] L. Cao, K. Klimes, Y. Ji, T. Fleetham, J. Li, *Nat. Photonics* **2021**, *15*, 230–237.
[24] H. Takeda, A. Kobayashi, K. Tsuge, *Coord. Chem. Rev.* **2022**, *470*, 214700.
[25] J.-G. Yang, X. Feng, N. Li, J. Li, X.-F. Song, M.-D. Li, G. Cui, J. Zhang, C. Jiang, C. Yang, K. Li, *Sci. Adv.* **2023**, *9*, eadh0198.
[26] M.-K. Sit, G. S. M. Tong, T.-L. Lam, G. Cheng, F.-F. Hung, K.-M. So, L. Du, K.-O. Choy, K.-H. Low, C.-M. Che, *Adv. Opt. Mater.* **2024**, *12*, 2302308.
[27] T.-Y. Li, S.-J. Zheng, P. I. Djurovich, M. E. Thompson, *Chem. Rev.* **2024**, *124*, 4332–4392.
[28] D. Di, A. S. Romanov, L. Yang, J. M. Richter, J. P. H. Rivett, S. Jones, T. H. Thomas, M. A. Jalebi, R. H. Friend, M. Linnolahti, M. Bochmann, D. Credgington, *Science* **2017**, *356*, 159–163.
[29] V. W.-W. Yam, A. S.-Y. Law, *Coord. Chem. Rev.* **2020**, *414*, 213298.
[30] M.-C. Tang, M.-Y. Chan, V. W.-W. Yam, *Chem. Rev.* **2021**, *121*, 7249–7279.

[31] J.-M. Kim, K. Cheong, J. Jiang, S. O. Jeon, W. P. Hong, J. Y. Lee, *Trends Chem.* **2023**, *5*, 267–278.
[32] Y. Chi, T.-K. Chang, P. Ganesan, P. Rajakannu, *Coord. Chem. Rev.* **2017**, *346*, 91–100.
[33] A. Bonfiglio, M. Mauro, *Eur. J. Inorg. Chem.* **2020**, *2020*, 3427–3442.
[34] G. Ni, J. Yan, Y. Wu, F. Zhou, P.-T. Chou, Y. Chi, *Inorg. Chem. Front.* **2023**, *10*, 1395–1401.
[35] H. Amouri, *Chem. Rev.* **2023**, *123*, 230–270.
[36] C. Wu, K. Shi, S. Li, J. Yan, Z.-Q. Feng, K.-N. Tong, S.-W. Zhang, Y. Zhang, D. Zhang, L.-S. Liao, Y. Chi, G. Wei, F. Kang, *EnergyChem* **2024**, *6*, 100120.
[37] X. Liang, Z.-L. Tu, Y.-X. Zheng, *Chem. Eur. J.* **2019**, *25*, 5623–5642.
[38] X. Tang, L.-S. Cui, H.-C. Li, A. J. Gillett, F. Auras, Y.-K. Qu, C. Zhong, S. T. E. Jones, Z.-Q. Jiang, R. H. Friend, L.-S. Liao, *Nat. Mater.* **2020**, *19*, 1332–1338.
[39] X. Zheng, R. Huang, C. Zhong, G. Xie, W. Ning, M. Huang, F. Ni, F. B. Dias, C. Yang, *Adv. Sci.* **2020**, *7*, 1902087.
[40] Y. Xin, Y. Zhu, R. Chi, C. Duan, P. Yan, C. Han, H. Xu, *Adv. Mater.* **2023**, *35*, 2304103.
[41] Y.-J. Yu, M. Song, X.-Y. Meng, Y.-K. Qu, X.-Q. Wang, L. Chen, S.-Y. Yang, D.-Y. Zhou, Z.-Q. Jiang, L.-S. Liao, *Org. Lett.* **2023**, *25*, 6024–6028.
[42] W. Yang, C. Xie, T. Chen, X. Yin, Q. Lin, S. Gong, Z. Quan, C. Yang, *Angew. Chem. Int. Ed.* **2024**, *63*, e202402704.
[43] C. You, X.-Q. Wang, X. Zhou, Y. Yuan, L.-S. Liao, Y.-C. Liao, P.-T. Chou, Y. Chi, *ACS Appl. Mater. Interfaces* **2021**, *13*, 59023–59034.
[44] J. Yan, Y. Xin, Y. Pan, G. Ni, S.-M. Yiu, Y. Chi, L. Duan, K. C. Lau, *Synth. Met.* **2024**, *308*, 117734.
[45] J. Yan, C. Wu, S.-M. Yiu, M. Kuhn, M. Huang, Y. Zhang, X. Zhou, C. Yang, G. Wei, Y. Chi, *Adv. Opt. Mater.* **2025**, *13*, 2402332.
[46] J. Yan, T. Nakamura, X. Tan, S.-M. Yiu, R. Mimura, K. Hoshi, X. Zhou, Y. Chi, H. Sasabe, J. Kido, *Chem. Eng. J.* **2024**, *488*, 150791.
[47] J. Yan, D.-Y. Zhou, L.-S. Liao, M. Kuhn, X. Zhou, S.-M. Yiu, Y. Chi, *Nat. Commun.* **2023**, *14*, 6419.
[48] J. Yan, Y. Pan, Z.-H. Qu, Z. Xu, K.-C. Law, D.-Y. Zhou, L.-S. Liao, Y. Chi, K.-C. Lau, *Adv. Photon. Res.* **2025**, *6*, 2400151.
[49] N. Tamosiunaite, L. C. Logie, S. E. Neale, K. Singh, D. L. Davies, S. A. Macgregor, *J. Org. Chem.* **2022**, *87*, 1445–1456.
[50] J. Yan, Y. Wu, I.-C. Peng, Y. Pan, S.-M. Yiu, K.-T. Wong, W.-Y. Hung, Y. Chi, K.-C. Lau, *J. Mater. Chem. C* **2023**, *11*, 12270–12279.
[51] J. Yan, Y. Pan, I. C. Peng, W.-Y. Hung, B. Hu, G. Ni, S.-M. Yiu, Y. Chi, K. C. Lau, *Inorg. Chem. Front.* **2024**, *11*, 2413–2426.
[52] J. Jin, Z. Zhu, J. Yan, X. Zhou, C. Cao, P.-T. Chou, Y.-X. Zhang, Z. Zheng, C.-S. Lee, Y. Chi, *Adv. Photon. Res.* **2022**, *3*, 2100381.
[53] Y. Qin, X. Yang, J. Jin, D. Li, X. Zhou, Z. Zheng, Y. Sun, W.-Y. Wong, Y. Chi, S.-J. Su, *Adv. Opt. Mater.* **2022**, *10*, 2201633.
[54] X. Yang, X. Zhou, Y.-X. Zhang, D. Li, C. Li, C. You, T.-C. Chou, S.-J. Su, P.-T. Chou, Y. Chi, *Adv. Sci.* **2022**, *9*, 2201150.
[55] G. Scalmani, M. J. Frisch, B. Mennucci, J. Tomasi, R. Cammi, V. Barone, *J. Chem. Phys.* **2006**, *124*, 094107.
[56] C. Adamo, D. Jacquemin, *Chem. Soc. Rev.* **2013**, *42*, 845–856.
[57] A. D. Laurent, C. Adamo, D. Jacquemin, *Phys. Chem. Chem. Phys.* **2014**, *16*, 14334–14356.
[58] R. L. Martin, *J. Chem. Phys.* **2003**, *118*, 4775–4777.
[59] T. Lu, F. Chen, *J. Comput. Chem.* **2012**, *33*, 580–592.
[60] Z. He, J. Li, D. Liu, H. Wan, Y. Mei, C. Shi, *J. Mater. Chem. C* **2022**, *10*, 18189–18199.
[61] D. Li, J. Yang, J. Chen, X. Peng, W. Li, Z. Chen, W. Qiu, G.-X. Yang, Z. Yang, M. Li, S. Jiang, D. Liu, Y. Gan, K. Liu, S.-J. Su, *Mater. Chem. Front.* **2023**, *7*, 1128–1136.
[62] X. Wang, H. Zou, H. Liu, Q. Mu, K. Zhang, Y. Xu, J. Fan, *Phys. Chem. Chem. Phys.* **2023**, *25*, 10977–10990.
[63] H. Zou, H. Liu, Q. Mu, K. Zhang, Y. Song, L. Lin, Y. Xu, C.-K. Wang, J. Fan, *Spectrochim. Acta A Mol. Biomol. Spectrosc.* **2023**, *285*, 121899.
[64] Y. Song, Y. Li, R. Yu, K. Zhang, L. He, *Adv. Opt. Mater.* **2023**, *11*, 2300432.
[65] T. Chen, Y. Xu, A. Ying, C. Yang, Q. Lin, S. Gong, *Angew. Chem. Int. Ed.* **2024**, *63*, e202401833.
[66] J. M. Younker, K. D. Dobbs, *J. Phys. Chem. C* **2013**, *117*, 25714–25723.
[67] P. Pander, A. V. Zaytsev, A. Sil, J. A. G. Williams, P.-H. Lanoe, V. N. Kozhevnikov, F. B. Dias, *J. Mater. Chem. C* **2021**, *9*, 10276–10287.
[68] P. Pander, L. Gomes Franca, F. B. Dias, V. N. Kozhevnikov, *Inorg. Chem.* **2023**, *62*, 5772–5779.
[69] J. Zhang, D. Ding, Y. Wei, F. Han, H. Xu, W. Huang, *Adv. Mater.* **2016**, *28*, 479–485.
[70] Y. Im, M. Kim, Y. J. Cho, J.-A. Seo, K. S. Yook, J. Y. Lee, *Chem. Mater.* **2017**, *29*, 1946–1963.
[71] U. Shakeel, J. Singh, *Org. Electron.* **2018**, *59*, 121–124.
[72] D. Berenis, G. Kreiza, S. Juršėnas, E. Kamarauskas, V. Ruibys, O. Bobrovas, P. Adomėnas, K. Kazlauskas, *Dyes Pigm.* **2020**, *182*, 108579.
[73] T. Azumi, C. M. O'Donnell, S. P. McGlynn, *J. Chem. Phys.* **1966**, *45*, 2735–2742.
[74] G. D. Hager, G. A. Crosby, *J. Am. Chem. Soc.* **1975**, *97*, 7031–7037.
[75] M. J. Leitl, V. A. Krylova, P. I. Djurovich, M. E. Thompson, H. Yersin, *J. Am. Chem. Soc.* **2014**, *136*, 16032–16038.
[76] M. Z. Shafikov, R. Martinscroft, C. Hodgson, A. Hayer, A. Auch, V. N. Kozhevnikov, *Inorg. Chem.* **2021**, *60*, 1780–1789.
[77] L.-Y. Peng, Z.-W. Li, G.-N. Pan, W.-K. Chen, Y.-J. Gao, G. Cui, *Phys. Chem. Chem. Phys.* **2023**, *25*, 6454–6460.
[78] P. Pander, A. Zaytsev, A. Sil, G. Baryshnikov, F. Siddique, G. Williams, F. B. Dias, V. N. Kozhevnikov, *Chem. Sci.* **2023**, *14*, 13934–13943.
[79] Y.-T. Lee, C.-Y. Chan, M. Tanaka, M. Mamada, U. Balijapalli, Y. Tsuchiya, H. Nakanotani, T. Hatakeyama, C. Adachi, *Adv. Electron. Mater.* **2021**, *7*, 2001090.
[80] H.-J. Cheon, S.-J. Woo, S.-H. Baek, J.-H. Lee, Y.-H. Kim, *Adv. Mater.* **2022**, *34*, 2207416.
[81] R. W. Weerasinghe, S. M. Suresh, D. Hall, T. Matulaitis, A. M. Z. Slawin, S. Warriner, Y.-T. Lee, C.-Y. Chan, Y. Tsuchiy, E. Zysman-Colman, C. Adachi, *Adv. Mater.* **2024**, *36*, 2402289.
[82] T. Hua, X. Cao, J. Miao, X. Yin, Z. Chen, Z. Huang, C. Yang, *Nat. Photonics* **2024**, *18*, 1161–1169.
[83] S. Nam, J. W. Kim, H. J. Bae, Y. M. Maruyama, D. Jeong, J. Kim, J. S. Kim, W.-J. Son, H. Jeong, J. Lee, S.-G. Ihn, H. Choi, *Adv. Sci.* **2021**, *8*, 2100586.
[84] R. Tang, S. Xu, L. Du, F.-F. Hung, T.-L. Lam, G. Cheng, K.-H. Low, Q. Wan, S. Wu, Y. Chen, C.-M. Che, *Adv. Opt. Mater.* **2023**, *11*, 2300950.
[85] Y. Tan, A. Ying, Y. Liu, X. Cai, L. Zhan, Z. Bin, J. You, C. Li, S. Gong, *Chem. Eng. J.* **2024**, *487*, 150618.
[86] K. Stavrou, L. G. Franca, A. Danos, A. P. Monkman, *Nat. Photonics* **2024**, *18*, 554–561.
[87] J. Yan, Z.-Q. Feng, Y. Wu, D.-Y. Zhou, S.-M. Yiu, C.-Y. Chan, Y. Pan, K. C. Lau, L.-S. Liao, Y. Chi, *Adv. Mater.* **2024**, *36*, 2305273.

Manuscript received: December 17, 2024
Revised manuscript received: March 01, 2025
Accepted manuscript online: March 11, 2025
Version of record online: March 24, 2025